Heliyon 9 (2023) e18496

Contents lists available at ScienceDirect

Heliyon

journal homepage: www.cell.com/heliyon

Nickel vanadate nitrogen-doped carbon nanocomposites for high-performance supercapacitor electrode

Awatif Rashed Z. Almotairy [a], Basheer M. Al-Maswari [b,c,*], Khaled Alkanad [d], N.K. Lokanath [d], R.T. Radhika [e], B.M. Venkatesha [c]

[a] Department of Chemistry, Faculty of Science, Taibah University, Yanbu 30799, Saudi Arabia
[b] Department of Chemistry, Faculty of Applied Sciences and Humanities, Amran University, Yemen
[c] Department of Chemistry, Yuvaraja's College, University of Mysore, Mysuru- 570005 Karnataka, India
[d] Department of Studies in Physics, University of Mysore, Manasagangotri, Mysuru 570 006, India
[e] Department of Chemistry, Maharani's Science College for Women, University of Mysore, Mysuru, India

ARTICLE INFO

Keywords:
Nickel vanadate
Nitrogen-doped carbon
Energy storage
Magnetic nanocomposites
Supercapacitor electrode

ABSTRACT

A nickel-vanadium-based bimetallic precursor was produced using the polymerization process by urea-formaldehyde copolymers. The precursor was then calcined at 800 °C in an argon ambiance to form a $Ni_3V_2O_8$-NC magnetic nanocomposite. Powerful techniques were used to study the physical characteristics and chemical composition of the fabricated $Ni_3V_2O_8$-NC electrode. PXRD, Raman, and FTIR analyses proved that the crystal structure of $Ni_3V_2O_8$-NC included N-doped graphitic carbon. FESEM and TEM analyses imaging showed the distribution of the $Ni_3V_2O_8$ nanoparticles on the layered graphitic carbon structure. TEM images showed the prepared sample has a particle size of around 10–15 nm with an enhanced active site area of 146 m^2/g, as demonstrated by BET analysis. $Ni_3V_2O_8$-NC nanocomposite exhibits magnetic behaviors and a magnetization saturation value of 35.99 emu/g. The electrochemical (EC) studies of the synthesized $Ni_3V_2O_8$-NC electrode proceeded in an EC workstation of three-electrode. In a 5 M potassium hydroxide as an electrolyte, the cyclic voltmeter exhibited an enhanced capacitance (C_S) of 915 F/g at 50 mV/s. Galvanic charge-discharge (GCD) study also exhibited a superior capacitive improvement of 1045 F/g at a current density (I_t) of 10 A/g. Moreover, the fabricated $Ni_3V_2O_8$-NC nanocomposite displays a good power density (P_t) of 356.67 W/kg, improved ion accessibility, and substantial charge storage. At the high energy density (E_t) of 67.34 W h/kg, the obtained P_t was 285.17 W/kg. The enhanced GCD rate, cycle stability, and E_t of the $Ni_3V_2O_8$-NC magnetic nanocomposite nominate the sample as an excellent supercapacitor electrode. This study paves the way for developing effective, efficient, affordable, and ecologically friendly electrode materials.

1. Introduction

In past decades, non-renewable energy sources have provided almost all human needs, but they intensify climate change by raising the temperature, hazardous compounds, and a variety of other problems [1,2]. In addition, population growth increases the energy demand, and the available resources are continuously decreasing, making it difficult to find a solution [3]. The rapid growth of the

* Corresponding author. Department of Chemistry, Faculty of Applied Sciences and Humanities, Amran University, Yemen.
E-mail address: basheer.almaswari@gmail.com (B.M. Al-Maswari).

https://doi.org/10.1016/j.heliyon.2023.e18496
Received 6 April 2023; Received in revised form 12 July 2023; Accepted 19 July 2023
Available online 20 July 2023

worldwide economy has led to a great interest in generating clean and efficient energy, especially in managing, storing, and producing this valuable energy [4–6]. Energy is humanity's most important concern due to its need in various fields. Given the exhaustion of available natural resources and the continued retrogradation of the environment over time, the call for efficient, sustainable, green energy alternatives and novel technologies for converting and storing the energies are vitally crucial and necessary [2,5–8]. In the realm of renewable energy, the growth potential is unparalleled. According to field experts, wind and solar are the most promising renewable energy sources for electricity generation [2,6]. However, they cannot be managed as necessary because they occur infrequently. Energy storage is a vital part of energy management and utilization, and it has been a great challenging scientific topic for industrially important. Turning chemical energy into electrical energy using novel electrochemical energy storage systems innovation has recently become a viable alternative to traditional sources [5]. Supercapacitors have received much attention in many applications, especially in energy storage owing to their desirable characteristics, including long-time charge storage, low cost, safety, and lightweight [9–11]. Supercapacitors are classified into two groups depending on their methods for storing electrical charge and the materials used for their electrodes: pseudocapacitors based on transition metal oxides and electrical double-layer capacitors (EDLC) based on carbon. Capacitance determination pseudocapacitors rely on rapid and continuous Faradaic redox processes which occur at or near the electrode surface.

In contrast, the capacitance determination in EDLC depends entirely on the buildup charges at the electrode interface [12–14]. More study has been done to develop electrode substances with structural properties and high reactivity for providing advanced electrochemical activity. Recently reported research suggested using mixed nanocomposites of transition-metal oxides owing to their many features, such as various oxidation states and their synergistic contributions, which would enhance the capacitive performance of the electrode [15,16]. It is well known that nickel vanadate was employed in supercapacitor applications because it is inexpensive, environmentally friendly, and naturally abundant. Moreover, it contains multiple vanadium valence states that enrich the composite structural makeup [17]. The application of nickel vanadate as a high-performance supercapacitor is significantly hampered by its low conductivity of electricity and change in volume extinction, resulting in a low consumption rate and quick power fading through the cycle. For instance, nanostructured $Ni_3V_2O_8$ of different morphologies as nanoparticles, nanowires, and nanorods, demonstrated great electrochemical utilization but insufficient stability [18–21]. Thus, further work is required to improve the stability and the use of active components. Using structures constructed of carbon matrix (C-matrix) containing nanomaterials, such as carbon pellets and carbon nanotubes to construct high-performance electrodes is an effective strategy [22,23]. However, recent researchers have revealed that introducing heteroatom nitrogen insertion into the carbon matrix may generate covalent polar connections among nitrogen and carbon atoms owing to their identical atomic size [24,25]. In addition, the bond between carbon and nitrogen exhibits greater strength than the bond between carbon and carbon due to the accelerated charge development between the nitrogen and carbon atoms [26–28]. Interestingly, a small amount of N-doping resulted in several local structures that are beneficial for improving electrical conductivity [26]. The n-doping technique has an impact on electrocatalysis and on other fields that deal with energy storage and energy conversion [29].

In this study, we used urea-formaldehyde copolymers to prepare N-doped carbon to combine with nickel vanadate to form $Ni_3V_2O_8$-NC as an electrode substance for supercapacitors to be used for energy storage. The $Ni_3V_2O_8$-NC magnetic nanocomposite achieved advanced *Cs* of 915 F/g at 50 mV/s in a 5 M potassium hydroxide through a cyclic voltmeter (CV). At an I_t of 10 A/g, a GCD study also showed an ultrahigh capacitive enhancement of 1045 A/g. The nano-size scale, excellent surface area, mesoporous framework, and large pore volume of the $Ni_3V_2O_8$-NC electrode contributed to its superior electrochemical efficiency. In addition, the $Ni_3V_2O_8$-NC electrode displays a good P_t of 356.67 W/kg, excellent ion accessibility, and substantial charge storage. The obtained P_t was found to be 285.17 W/kg at a high E_t of 67.34 W h/kg.

2. Experiments

2.1. Materials

The precursors were bought from Sigma Aldrich grade and experimented as supplied; the manufacture of $Ni_3V_2O_8$-NC magnetic nanocomposite involved the use of the chemicals sodium hydroxide (NaOH), urea (purity 99%), formaldehyde (purity 37% aqueous solution), Ni $(NO_3)_2{\cdot}6H_2O$ (purity 99.999%), and NH_4VO_3 (purity 99.95%).

2.2. Fabrication of $Ni_3V_2O_8$-NC magnetic nanocomposite

The $Ni_3V_2O_8$-NC magnetic nanocomposite was synthesized using the polymerization technique to create the precursors [27,28]. In the first step, the salts mixture consisting of (5.8 g (0.02 mol) of Ni $(NO_3)_2{\cdot}6H_2O$ was dissolved with 2.334 g (0.02 mol) of NH_4VO_3 in 40 ml of double distilled H_2O), labeled as M-1. At the same time, a mixture of formaldehyde (10 ml, 0.2 mol, 37% aqueous solution) and urea (6.0 g, 0.1 mol) was combined at pH 8–10 (NaOH was utilized for the adjustment) and labeled as M-2. The resulting suspension mixture (M − 2) was then stirred at 70 °C for 1 h to create the urea-formaldehyde (UF) polymer ligand. In the second step, the M − 1 was blended with the M − 2 for 4 h at 70 °C, forming a polymeric of two metals named NiV_2-UF. Subsequently, the resulting NiV_2-UF was meticulously washed multiple times using distilled H_2O and ethanol before being dried at 50 °C. To yield the $Ni_3V_2O_8$-NC magnetic nanocomposite, the NiV_2-UF precursors were subjected to calcination at 800 °C in an argon chamber ambiance, with a 5 °C/min heating rate for 4 h. Scheme 1 illustrates the process of preparing the targeted nanocomposite.

2.3. Electrochemical experiments

CHI 608e electrochemical (EC) workstation of three electrodes program was applied to explore the EC properties of the fabricated $Ni_3V_2O_8$-NC magnetic nanocomposite. 0.004 ml of Nafion aqueous, 2 ml of isopropanol, and about 3 mg of the prepared $Ni_3V_2O_8$-NC sample were sonicated for 20 min. Approximately 0.05 ml of the mixture was loaded on the glassy carbon and desiccated in an enclosed vacuum chamber at 50 °C. The coated mass of the sample on the glassy carbon electrode was nearly 0.075 mg [5,30,31]. In this experiment, the counter electrode was the Pt wire, the reference electrode was the Ag/AgCl, and a potassium hydroxide (KOH) solution (5 M) was the electrolyte. Various studies, such as CV, GCD, and EC impedance spectroscopy (EIS), were investigated. The EIS analysis involved conducting tests in an open circuit, applying an alternating current (AC) voltage with an amplitude of 5 mV. The frequencies ranged from 10 kHz to 0.1 MHz.

2.4. Characterization techniques

The elements' oxidation states were studied using the XPS technique by the PHI 5000VersaProbe III. The Raman spectrum of $Ni_3V_2O_8$-NC magnetic nanocomposite was obtained using a Raman confocal (WITec alpha 300RA) microscope. The magnetization properties have been investigated at ambient conditions using a vibrating sample magnetometer (VSM) (7410 Series VSM). The Bruker Tensor II spectrometer obtains the Fourier-transferred infrared (FTIR) fingerprints ranging from 400 to 4000 cm^{-1}. The thermogravimetric analyzer (TGA) analysis of the produced $Ni_3V_2O_8$-NC magnetic nanocomposite was performed using an SII 6300 EXSTAR at 10 °C/min reaction temperature and the differential thermal (DTA) as well attached to the TGA. The surface area for $Ni_3V_2O_8$-NC magnetic nanocomposite was determined by the Tristar II Plus (BET Micromeritics analyzer). The crystalline phase of obtained $Ni_3V_2O_8$-NC was confirmed using an X-ray diffractometer (Rigaku- = 1.54059, Cu–K radiation). The morphology of the $Ni_3V_2O_8$-NC was determined using high-resolution scanning electron microscopy (FESEM, JSM-7600F) and transmission electron microscopy (TEM, Tecnai G2, F30).

3. Results and discussions

XPS analysis was employed to find the elemental components responsible for the composition of the $Ni_3V_2O_8$-NC magnetic nanocomposite. Fig. 1a shows that $Ni_3V_2O_8$-NC contained nickel, vanadium, oxygen, carbon, and nitrogen elements on the surface of the magnetic nanocomposite. On the other side, Fig. 1b displays the high-resolution-XPS (HR-XPS) of N 1s, fitted into three peaks indexed for graphite-N at binding energy (400.22 eV), pyrrolic-N at binding energy (399.31 eV), and pyridinic-N at (398.42 eV) [27,

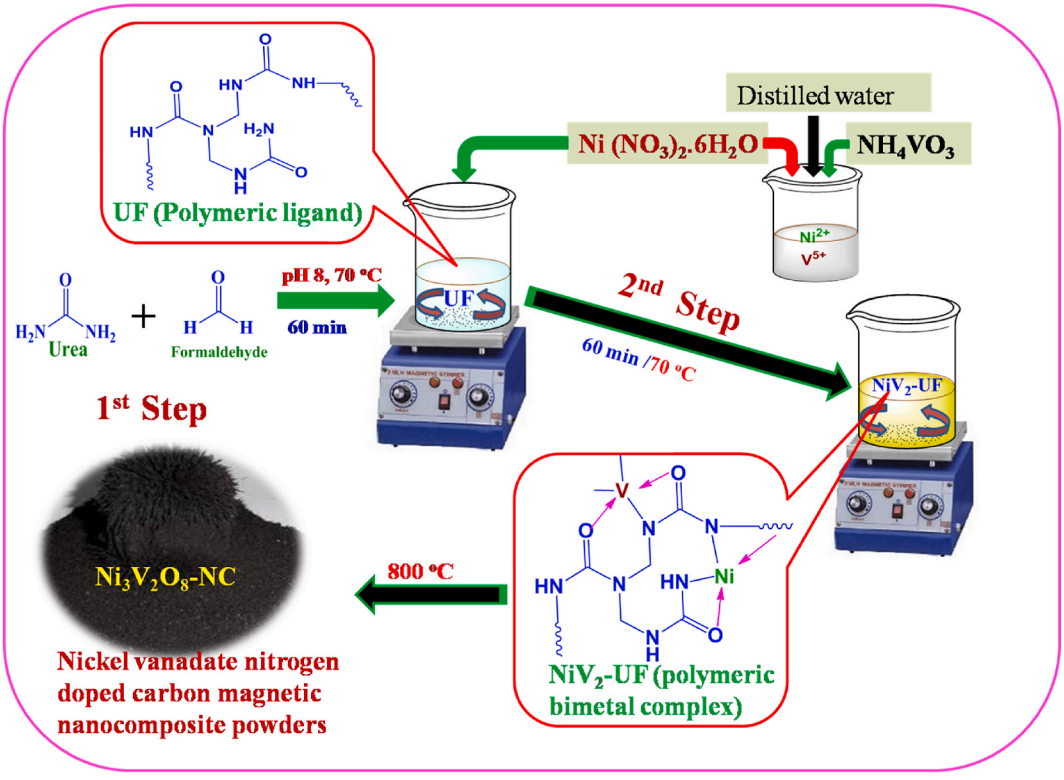

Scheme 1. Systematic preparation of $Ni_3V_2O_8$-NC magnetic nanocomposite.

28,32,33]. The presence of pyrrolic-N in $Ni_3V_2O_8$-NC magnetic nanocomposite ensures a high electrical conductivity for the sample [34]. Fig. 1c illustrates that $Ni_3V_2O_8$-NC has a sharp HR-XPS of the C 1s spectrum at 284.82 eV credited to C=C/C–C [35]. C 1s core level has been further fitted to three peaks at 286.87 and 290.21 eV are congruent with C–N/C=N and O–C=O, respectively, and 292.51 eV is most likely assigned for C=O [36]. The XPS O 1s peak (Fig. 1d) demonstrated three fitted peaks at 532.92, 530.81, and 529.71 eV corresponding to the C–OH surface group, V–O bonds, and Ni–O, respectively [32,36]. The Ni 2p HR-XPS spectrum of $Ni_3V_2O_8$-NC magnetic nanocomposite exhibits four peaks (Fig. 1e). The prominent peaks at 871.64 eV and 855.38 eV are credited to Ni $2p_{1/2}$ and Ni $2p_{3/2}$, respectively. Additional two low-intensity shoulders located at 860.87 eV and 880.18 eV are satellites accredited to Ni $2p_{3/2}$ and Ni $2p_{1/2}$, respectively; this denotes the type of nickel vibration located at the higher binding energy. These four peaks of Ni 2p show that the $Ni_3V_2O_8$-NC magnetic nanocomposite is in the Ni^{2+} valence state [27,32]. Fig. 1f demonstrates two peaks in the HR-XPS spectrum attributed to V 2p, the peak at 516.73 eV credited to V $2p_{3/2}$ and the other at 523.85 eV, attributed to V $2p_{1/2}$. These two peaks reveal that the $Ni_3V_2O_8$-NC magnetic nanocomposite contains vanadium in a valence state of +5 [32,37].

Fig. 2a displays the Raman scattering spectrum of the $Ni_3V_2O_8$-NC magnetic nanocomposite. The compositional characteristics of the materials and the formation of graphite carbon were investigated. The graphite G bands and the D defect were found to be related to the double vibrational peaks located at 1348 and 1589 cm^{-1}, respectively. The band G is generated by the E_{2g} phonon, which is present in C sp^2 hybridized atoms, whereas the D band is produced by the k-point phonons, which have A_{1g} symmetry [27,33,37,38]. The $Ni_3V_2O_8$-NC magnetic nanocomposite has a band intensity ratio (I_D/I_G = 1.59). This value demonstrates the high quality of the graphite, which has pores and vacant positions in the carbon matrix. These porosities enhance the active site area of the $Ni_3V_2O_8$-NC, increasing the charge transport activity while boosting charge storage mobility and structural robustness, which are essential for energy storage [28]. The peaks that appeared at 332-480 cm^{-1} are ascribed to the stretching of V–O–V bonds. In contrast, $Ni_3V_2O_8$-NC has shown a peak at 815 cm^{-1} that can be credited to V–O tetrahedral's distortion and bending vibration, which matches the reported literature [37–42]. The Raman spectrum clearly showed that $Ni_3V_2O_8$-NC magnetic nanocomposite was successfully formed. Fig. 2b illustrates the magnetic properties of the fabricated $Ni_3V_2O_8$-NC magnetic nanocomposite using VSM analysis (at room temperature with applied magnetic fields of ±20 kOe). The investigation was carried out to determine the coercivity (H_C), saturation magnetization (M_S), and remnant magnetization (M_R). It was found that M_S, H_C, and M_R have the value of 35.99 emu/g, 292.33 Oe, and 10.47 emu/g, respectively.

The molecular structure of the fabricated NiV_2-UF precursor and $Ni_3V_2O_8$-NC magnetic nanocomposite has been studied and compared using FTIR spectroscopy (Fig. 3a). Before calcination, the configuration derived a distinct FTIR spectrum of NiV_2-UF

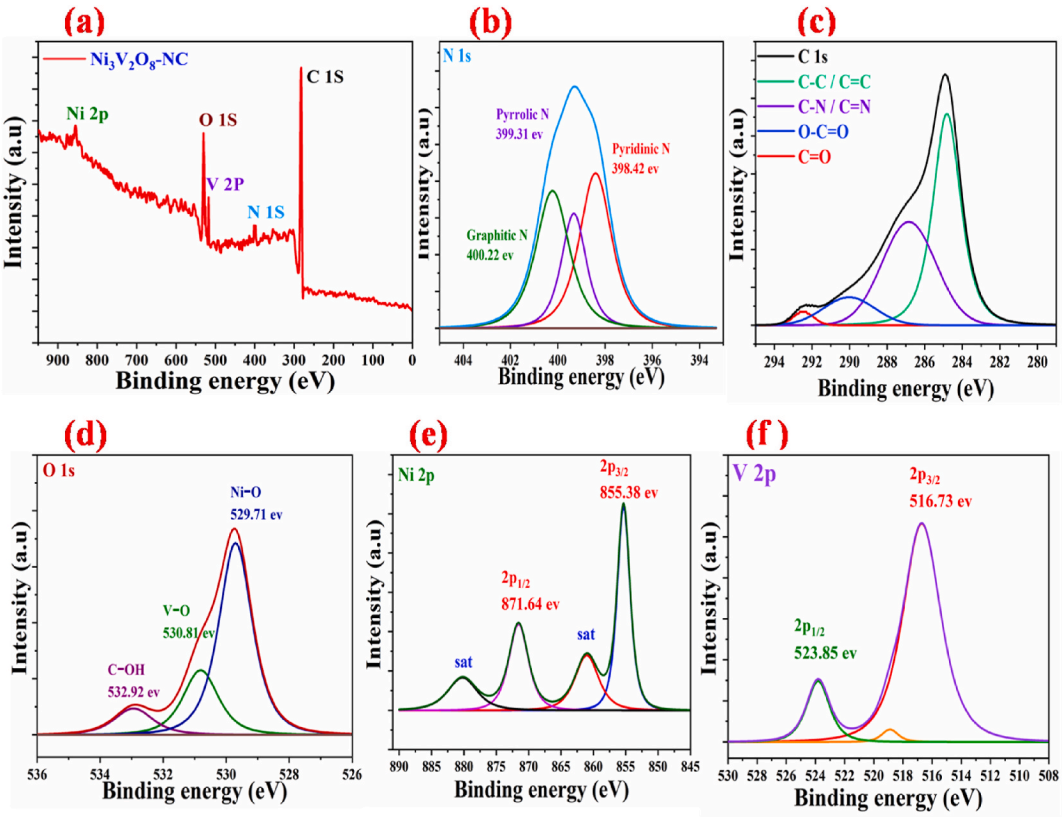

Fig. 1. (a) XPS comprehensive survey spectrum, and HRXPS of (b) N 1s, (c) C 1s, (d) O 1s, (e) Ni 2p, and (f) V 2p of $Ni_3V_2O_8$-NC magnetic nanocomposite.

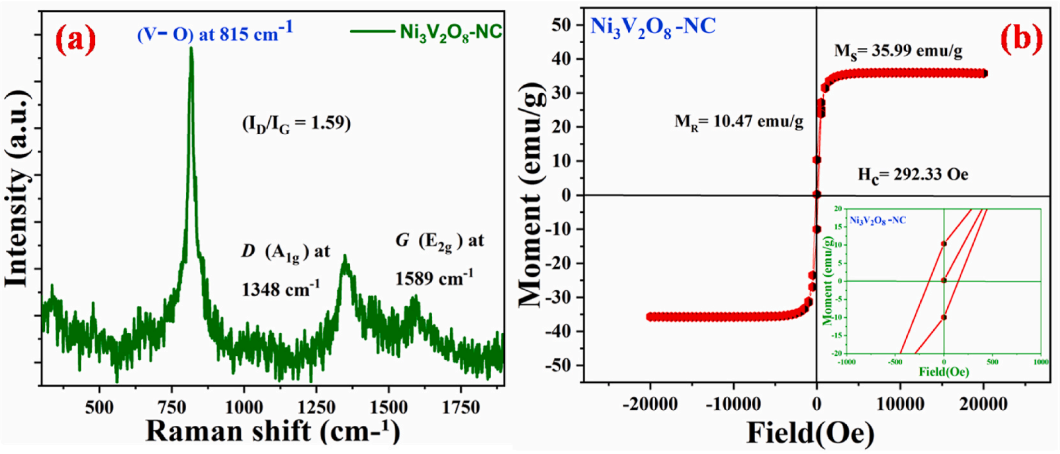

Fig. 2. (a) Raman analysis, and (b) VSM curve of $Ni_3V_2O_8$-NC magnetic nanocomposite.

complex between 1700 and 1200 cm^{-1} and aromatic C–N heterocycles in the stretched mode, with the C=C and C=N stretch modes located at 1577 and 1640 cm^{-1}, respectively, where the aromatic C–O and C–N vibratory stretching modes, and the C–H bending are located at 1234–1317, 1404, and 1461 cm^{-1}, respectively [27,33,43,44]. A solid fingerprint at 818 cm^{-1} and a minimal one at 881 cm^{-1} were observed, attributed to the distinct beaks in the graphic carbon nitride [44], where the shift in these bonds is due to their overlapping with the stretching vibrational band of the V–O group [45,46]. The peaks in the region between 3079 and 3465 cm^{-1} resulted from stretching the N–H and O–H bonds, respectively [2,28,33,43]. The specific vibratory peak at 465 cm^{-1} designates the existence of the Ni–O vibrational mode, whereas the band at 690 cm^{-1} is accredited to the Ni–O–H vibratory stretching mode [45,47,48]. However, most of the FTIR bands (C–H, N–H, and O–H) vanished, whereas the C–N and C–O bonds were reduced, and the bands of the metal oxide were prominent (Fig. 3a) [27]. As a consequence of the breakdown of the NiV_2-UF during the calcination process, the chemical structure of NiV_2-UF changed to $Ni_3V_2O_8$-NC magnetic nanocomposite.

The carbon content of the $Ni_3V_2O_8$-NC magnetic nanocomposite was measured by thermogravimetric analysis (TGA) under atmospheric conditions. The results revealed four phases of the thermal breakdown (Fig. 3b). In the first stage, the presence of moisture caused a mass loss of 5.68% between 25 and 140 °C. The next phase is characterized by a 13.21% weight loss owing to the oxidative breakdown of organic materials at (140–350 °C), and the thermal deterioration of carbon graphite during the third phase led to a weight loss of 32.47% at (350–650 °C). In the fourth phase, other organic components caused a weight loss of 25.35% between 650 and 800 °C [27,28,33,42]. As predicted, Fig. 3b shows the DTA curve has three peaks, indicating the fabricated $Ni_3V_2O_8$-NC magnetic nanocomposite was formed by exothermic processes. The peak at 326 °C represents organic weight loss and the disintegration of the gel structural system, whereas the peak at 632 °C represents carbon dioxide release. $Ni_3V_2O_8$-NC exhibits a peak at 730 °C, which is above the Néel temperature, indicating the transformation of the martial from antiferromagnetic to paramagnetic [49,50].

N_2 adsorption/desorption isotherms measurement for the $Ni_3V_2O_8$-NC magnetic nanocomposite was done to study the specific

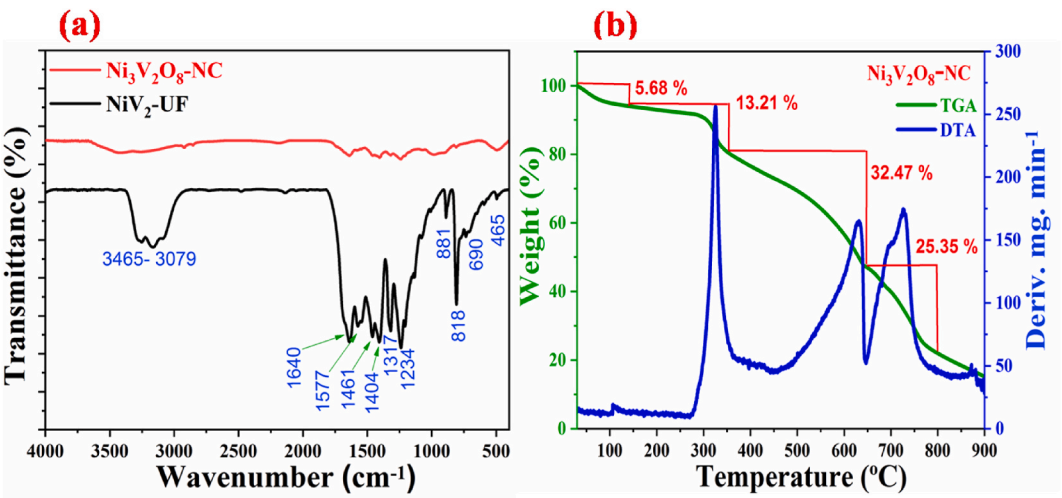

Fig. 3. (a) FT-IR bands of the NiV_2-UF and $Ni_3V_2O_8$-NC, (b) TGA/DTG of $Ni_3V_2O_8$-NC magnetic nanocomposite.

active surface and the porous structure of the composite [51]. Fig. 4a demonstrates the hysteresis loops attributed to the IV isothermal type, which ensure a typical mesoporous structure of the sample [52,53]. The distribution of the mesoporous was estimated using the BJH model and calculated to be ~3.3287 nm (Fig. 4a). The calculated BET-specific area of $Ni_3V_2O_8$-NC was around 146 m^2/g. The carbon matrix contains numerous interconnected pyramidal pores and long-winding hollow channels, which are crucial in retaining and facilitating access to electrolytes. Two key factors enhance the rate of electrochemical energy storage. Firstly, the enhanced surface area increased the number of active sites. Secondly, mesoporous structures enable the highly efficient transfer of electrolyte ions [28, 42,54]. The structure and crystallinity of the $Ni_3V_2O_8$-NC magnetic nanocomposite were confirmed using PXRD. Fig. 4b showed the exesitnce of the nitrogen-doped graphitic carbon in the strucuture of $Ni_3V_2O_8$-NC, which clearly assigns in the miller levels (002) and (100) at 2θ of 25.17° and 43.75, respectively [11,27,28,33,54–56]. Fig. 4b showed that the strong and maximum intense XRD peaks at 35.73° and 44.07° attributed to (221) and (240) planes, respectively, attributed to the $Ni_3V_2O_8$ (JCPDS card No. 70–1394) [3,23,57]. It is well known that at a higher calcination temperature, the nickel-vanadium phase would transfer to other phases [58]. Therefore, the minor peaks could be assigned for the residuals of different nickel-vanadium phases, mainly corresponding to the $Ni_2V_2O_6$ (ICSD #3388) [59]. XRD results are in line with Raman and FTIR analyses.

The FESEM was used to examine the morphology of the fabricated $Ni_3V_2O_8$-NC electrode. Fig. 5 shows the composite has a layered structure embedded with an irregular aggregation of nanoparticles. This irregular agglomeration of nanoparticles might be owed to the energy of the sample's surface and magnetic properties [60]. Elemental mapping of the $Ni_3V_2O_8$-NC is shown in Fig. 5, demonstrating Ni, V, O, C, and N are the elements of the nanocomposite construction.

Fig. 6a and b displays the TEM images of the $Ni_3V_2O_8$-NC; the grains/particles size was calculated to be about 10–15 nm. HR-TEM images illustrate the high crystallinity of the prepared $Ni_3V_2O_8$-NC magnetic nanocomposite. Fig. 6c and d shows that there are two different d-spacing to be 0.354 nm assigned for (002) and 0.204 nm given for (240) miller levels, which belong to graphitic carbon matrix and $Ni_3V_2O_8$, respectively [23,33]. Hence, the HR-TEM finding is well-matched with XRD analysis. The selected area electron diffraction (SAED) configuration for $Ni_3V_2O_8$-NC displays two condensed circles pointed as (221) and (240) of the miller levels of $Ni_3V_2O_8$ and one circle pointed as (002), which is assigned to the graphite carbon (Fig. 6e). Henceforth, the SAED pattern of $Ni_3V_2O_8$-NC indicates the nanostructure is strongly linked with the graphite carbon framework. SAED pattern of $Ni_3V_2O_8$-NC demonstrates that the $Ni_3V_2O_8$ nanostructure is firmly complexed with the N-doped graphite carbon structure. As a result, the SAED result is well in agreement with HR-TEM and XRD analyses. The presence of ordered cycles and dots in the SAED image provides evidence of the crystalline nature of the prepared nanocomposite, promoting long-term structural stability. This architecture undoubtedly greatly enhances the electrochemical performance, making it highly efficient for supercapacitor applications [61].

4. Electrochemical performance

It is well-established that the structure and morphology of the nanocomposite determine the electrochemical electrode's performance, and its increased surface area accelerates the intercalation phenomenon [62]. A three-electrode program was performed to study the EC properties of the $Ni_3V_2O_8$-NC magnetic nanocomposite. The EC activity of $Ni_3V_2O_8$-NC magnetic nanocomposites as an electrode for storing the energy (Fig. 7). Various scan rates between 50 and 200 mV/s were used to determine the CV of $Ni_3V_2O_8$-NC with KOH 5 M as the electrolyte solution. The voltage range of operation was between (−0.45 and + 0.45 V), as displayed in Fig. 7a. The CV displayed no noticeable redox peaks, implying that its characteristics are similar to those of a standard double-layer capacitor (Fig. 7a). There were found semi-rectangular shapes without oxidation peaks. Redox peaks are absent due to the constant charging and

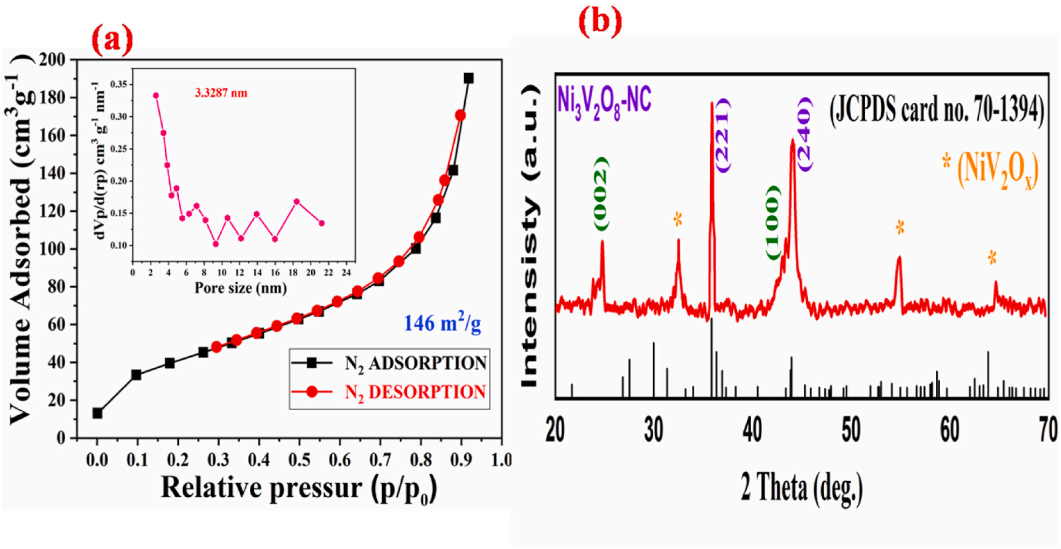

Fig. 4. (a) BET surface area of the $Ni_3V_2O_8$-NC (b) XRD patterns of $Ni_3V_2O_8$-NC magnetic nanocomposite.

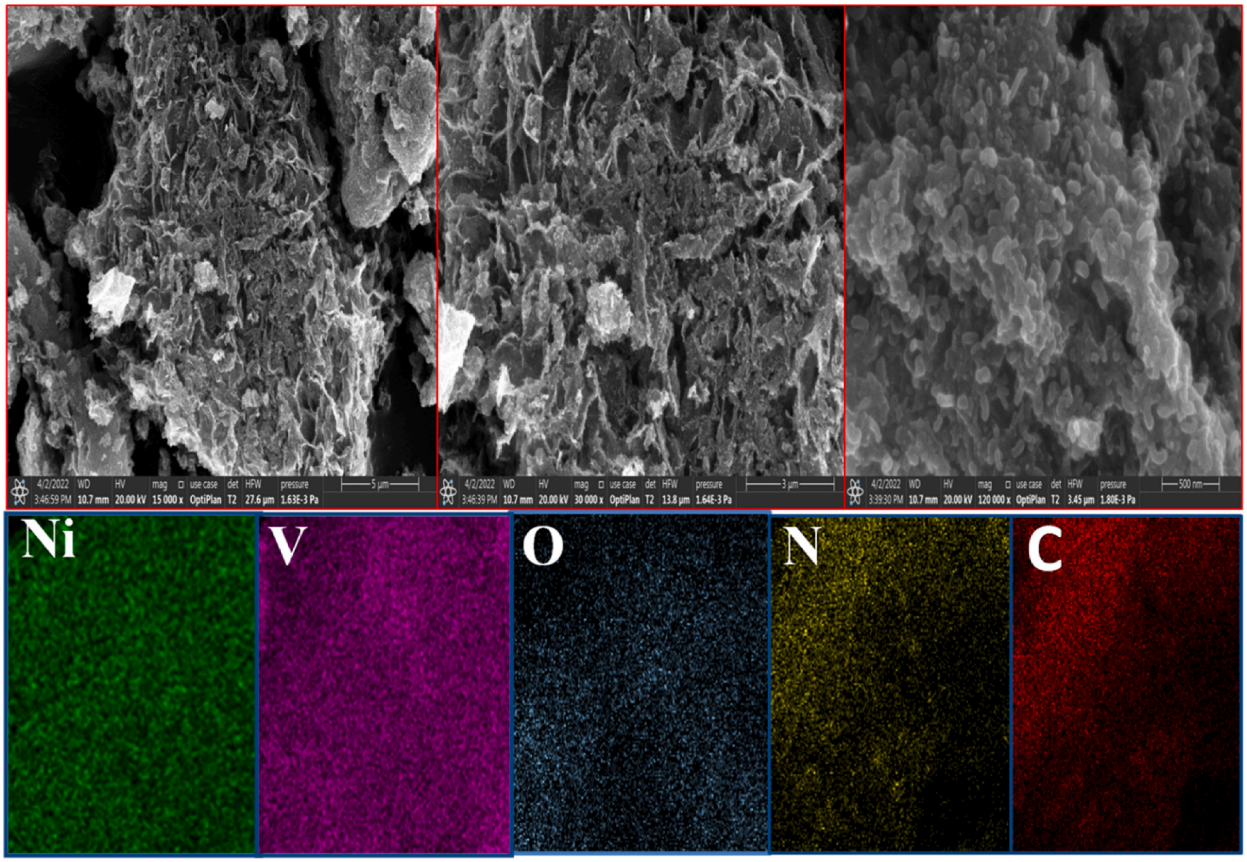

Fig. 5. FESEM and elemental mapping images of $Ni_3V_2O_8$-NC magnetic nanocomposite.

discharging rate during the cycle [63,64]. The C_S of the $Ni_3V_2O_8$-NC magnetic nanocomposites was calculated using Equation (1) and estimated to be around 915 F/g at 50 mV/s; the plot of the value (C_S) *vs* diverse scan rates from the CV curve is illustrated in Fig. 7b.

$$C_s = \frac{\int I(V)dV}{m \times \Delta V \times v} \quad (\mathrm{F/g}) \tag{1}$$

Where m (mg) is the active mass of the composite, ΔV (V) is the potential window, $\int I\,(V)\,dV$ symbolizes the area obtained from the (CV) curve, and ν (V/s) is the scan rate. Electric double-layer capacitors (EDLC) performance is confirmed by the EC response in CV (Equations (2)–(5)). This performance is owing to the intricate interplay between the electrode's interface and the electrolyte ions within the sample porosity.

$$Ni_3V_2O_8 + 12\ OH^- \rightarrow 2VO_4 + 3NiO_2 + 6H_2O + 12\ e^- \tag{2}$$

$$Ni^{2+} + 2OH^- \rightarrow Ni\ (OH)_2 \tag{3}$$

$$4\ Ni\ (OH)_2 + 2e^- \rightarrow 3NiO + 3H_2O + 2OH^- + Ni^{(0)} \tag{4}$$

$$Ni^{(0)} + 4OH^- \leftrightarrow NiO_2 + 2H_2O + 4e^- \tag{5}$$

The GCD studies were also conducted between voltages (0–0.7 V) at different CDs from 10 to 50 A/g, as displayed in Fig. 7c. Equation (6) was employed to determine the C_S of the electrode (for the three-electrode program) relying on GCD rates of the $Ni_3V_2O_8$-NC magnetic nanocomposites at different I_t [33,63].

$$C_s = \frac{I \times \Delta t}{m \times \Delta V} \quad \mathrm{F}\Big/\mathrm{g} \tag{6}$$

Where I (mA) discharge current and Δt (s) is the discharge time. The C_S values were found to be 1045, 715.44, 502.6, 321.83, and 197.76 F/g for I_t of 10, 20, 30, 40, and 50 A/g, respectively. According to the GCD of the $Ni_3V_2O_8$-NC magnetic nanocomposites, the highest value for C_s is around 1045 F/g at 10 A/g. With the raising of the I_t from 10 A/g to 50 A/g, the *Cs* of the $Ni_3V_2O_8$-NC magnetic nanocomposite reduced from 1045 to 197.76 F/g (Fig. 7d). The P_t, E_t, and specific capacitance of the symmetric electrode (C_t) are

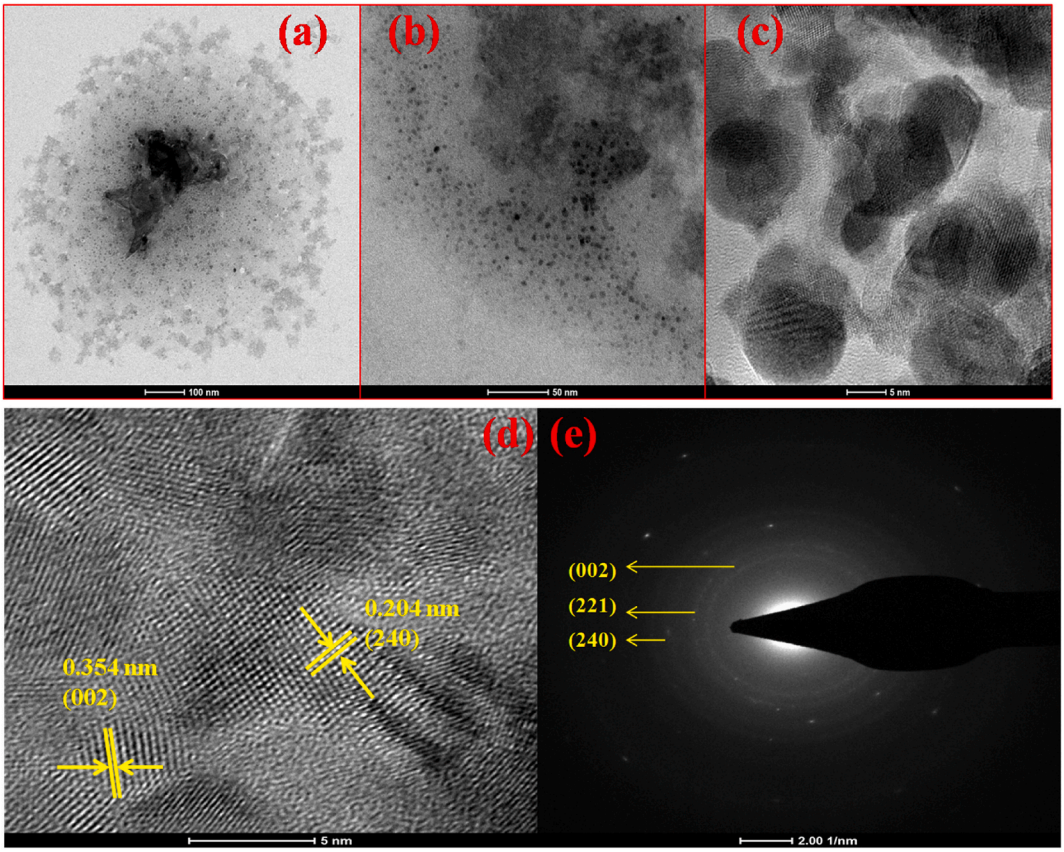

Fig. 6. (a, b) TEM, (c, d) HR-TEM, and (e) SAED images of the $Ni_3V_2O_8$-NC magnetic nanocomposite.

measured by a two-electrode testing system using the bellow Equations (7)–(9):

$$C_t = \frac{4I \times \Delta t}{m \times \Delta V} \quad \mathrm{F}\Big/\mathrm{g} \tag{7}$$

$$E_t = \frac{1}{8 \times 3.6} \mathrm{C_t} \Delta V^2 \quad \mathrm{Wh}\Big/\mathrm{kg} \tag{8}$$

$$P_t = \frac{E_t}{\Delta t} \times 3600 \quad \mathrm{W}\Big/\mathrm{kg} \tag{9}$$

The symmetric cell showed E_t values of approximately 67.34, 46.11, 32.39, 20.74, and 12.74 W h/kg at P_t of 285.15, 291.22, 300.84, 314.42, and 356.67 W/kg, respectively. Decreasing the E_t values from 67.34 to 12.74 W h/kg, the P_t increased from 285.15 to 356.67 W/kg. Therefore, the $Ni_3V_2O_8$-NC magnetic nanocomposite exhibits exceptional P_t and E_t, which is vital for environmental sustainability and commercial viability [65].

Fig. 8a illustrates the EIS finding, depicted as Nyquist frequency for the $Ni_3V_2O_8$-NC composite. The curve was generated within 10 Hz to 0.1 MHz (the frequency), with an AC and an amplitude of 5 mV. The Nyquist plot shows two distinct components: a semicircular feature and a linear section depicting the Warburg impedance (Z_w) and the charge transfer resistance (R_{ct}) associated with the electrolyte and electrode junction. The semicircle's diameter determines the electrode material's interfacial resistance R_{ct} influences. The internal resistance (R_s) can be calculated using the actual axis intercept, which leans on the contact and electrolyte resistance [18,33,63]. The EIS spectrum and the equivalent circuit model can be seen in Fig. 8a. The circuit consists of the EDLC, C_{dl}, R_s, R_{ct}, and Z_w. For $Ni_3V_2O_8$-NC magnetic nanocomposites, the values were R_s and R_{ct} at roughly 20.49 and 19.49 Ω, whereas Z_w was valued at approximately 2.7 kΩ. These values indicate excellent conductivity and stability of the prepared electrode [63,66,67]. The comparison of the current work with earlier studies is shown in Table 1. Our material demonstrates notable electrochemical performances for supercapacitors for energy storage. For example, the studied sample showed about three times higher specific capacitance than reported graphene/nickel vanadate ($Ni_3V_2O_8$) and $Ni_3V_2O_8$@GO [45,68].

The GCD performance was carried out to assess the cyclic proficiency of the $Ni_3V_2O_8$-NC electrode at an I_t of 50 A/g, as depicted in Fig. 8b. The C_s gradually decrease throughout the cyclic process due to the electrode materials' activation process [41,63,74]. Even

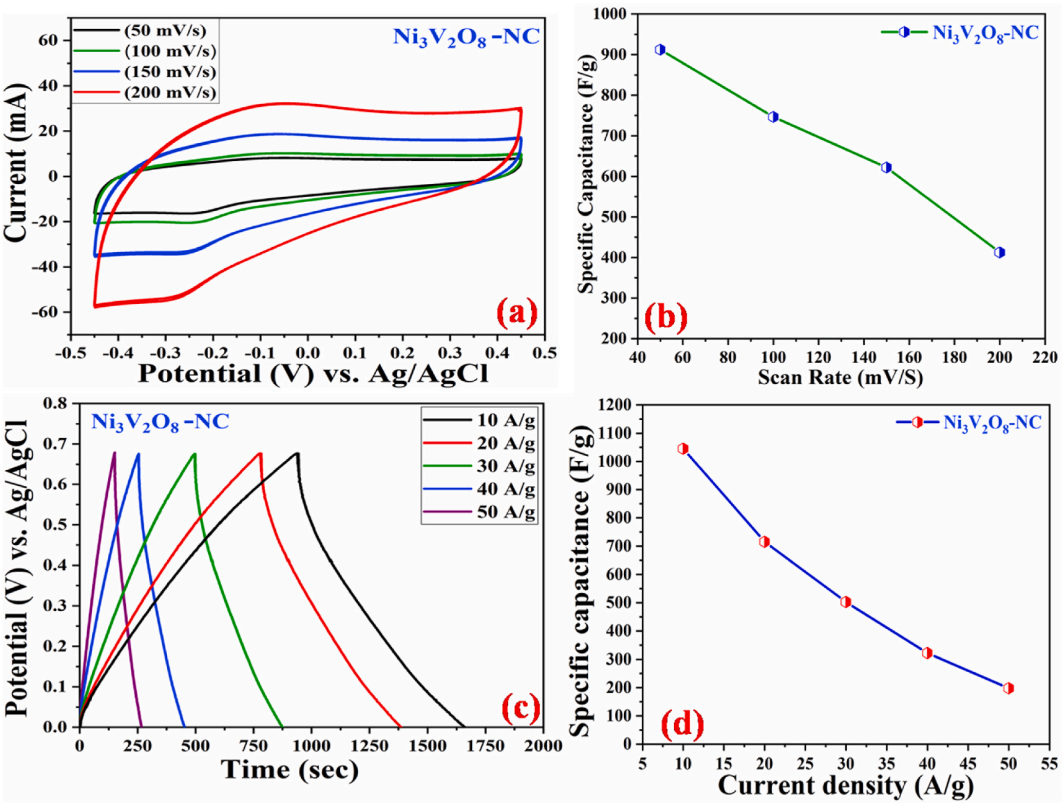

Fig. 7. EC analyses of $Ni_3V_2O_8$-NC magnetic nanocomposites (a) CV, (b) Cs by CV (c) GCD, and (d) Cs by GCD.

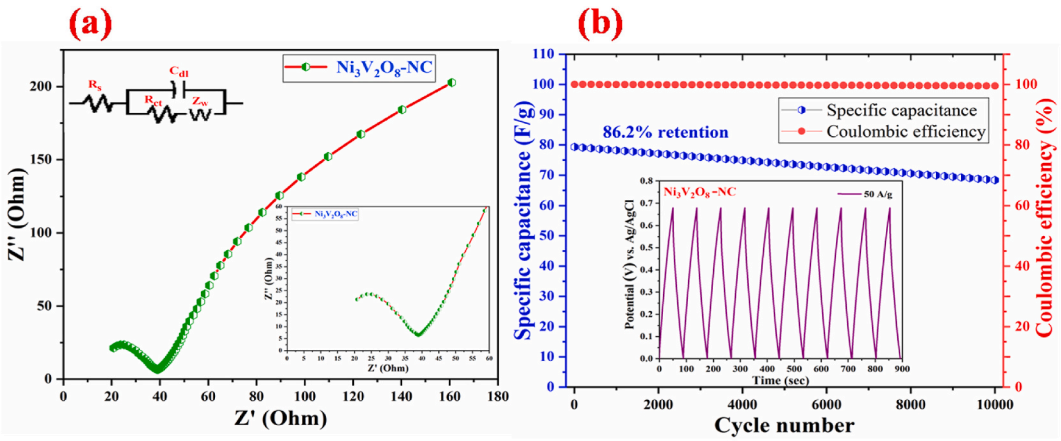

Fig. 8. (a) EIS curve of the $Ni_3V_2O_8$-NC magnetic nanocomposites and (b) C_s and Coulombic efficiency against cycle number by the $Ni_3V_2O_8$-NC magnetic nanocomposite in the inset presents the last 10 GCD curves.

after 10,000 cycles, the device demonstrates remarkable cyclic stability, with 86.2% retention of its original C_s (as shown in the inset figure displaying the last 10 GCD cycles). We attribute this exceptional cyclic stability primarily to the morphology and structure of the $Ni_3V_2O_8$-NC magnetic nanocomposite. The Coulombic efficiency has been established for the $Ni_3V_2O_8$-NC nanocomposite and measured to be 99.5% after 10,000 cycles at 50 A/g scan rate. These outcomes further confirm the sample's proficiency as a supercapacitor device. However, the fabricated $Ni_3V_2O_8$-NC electrode's EC behavior is primarily owing to its high porosity and specific active surface area, as shown in Fig. 4a.

Table 1
Comparing the current work to earlier reports of EC performances for energy storage and supercapacitors.

Electrode type	Electrolyte	I_t (A/g)	E_t (W h kg^{-1})	P_t (W kg^{-1})	C_S (F/g)	References
$Ni_3V_2O_8$	4 M KOH	5	32.98	189.96	263.12	[3]
$NiFe_2O_4$	2 M KOH	5	10.4	225.8	478	[69]
porous graphene-NiO (PGNO)	2 M KOH	5	13.4	225	511	[70]
$Ni_3V_2O_8$	6 M KOH	5	17.4	250	118	[45]
Graphene/$Ni_3V_2O_8$	2 M KOH	0.5	103.94	45,610	748	[38]
Graphene-$Zn_3V_2O_8$	2 M KOH	0.8	78	75,500	564	[12]
$Co_3V_2O_8$	2 M KOH	0.6	–	–	505	[52]
$Ni_3V_2O_8$@GO	6 M KOH	5	17.4	250	296	[45]
$Ni_3(VO_4)_2$	6 M KOH	1	25.3	240	402.8	[71]
NiV_2O_6/C	2 M KOH	10	–	–	682	[59]
graphene/nickel vanadate ($Ni_3V_2O_8$)	6 M KOH	0.5	51	920	368	[68]
NF@NCO	3 M KOH	0.2	61.2	371.5	1018	[72]
NCFC − NCs	5 M KOH	5	–	–	474	[73]
$Ni_3V_2O_8$ -NC magnetic nanocomposite	**5 M KOH**	**10**	**67.34**	**356.67**	**1045**	**Present**

5. Conclusion

The $Ni_3V_2O_8$-NC magnetic nanocomposite was produced using the polymerization technique at 800 °C for 4 h with a size of about 10–15 nm. BET analysis showed the $Ni_3V_2O_8$-NC magnetic nanocomposite feature with a great specific active surface of 146 m^2/g. FTIR, XRD, and Raman analyses investigated the structure of the $Ni_3V_2O_8$-NC. FESEM and TEM explore the morphology and grain size of the sample. VSM demonstrated the $Ni_3V_2O_8$-NC exhibited excellent magnetic characteristics with a Ms = 35.99 emu/g. The $Ni_3V_2O_8$-NC electrode displayed an improved C_S of 915 F/g at 50 mV/s by CV in a 3-electrode program. Additionally, GCD analysis display enhanced capacitive performance (Cs = 1045 F/g) at an I_t of 10 A/g. The maximum E_t of the replica cell was obtained at 67.34 W/kg with an E_t of 285.17 W/kg before dropping to 12.74 W/kg with a P_t of 356.67 W/kg. After 10,000 cycles, the electrode displays 86.2% retaining its original capacitance, showing excellent cyclical stability. The Coulombic efficiency has been confirmed for the $Ni_3V_2O_8$-NC electrode and measured to be 99.5% after 10,000 cycles at a rate scanning equal to 50 A/g. The nitrogen-doped graphitic carbon was shown to have a synergistic effect that increased conductivity while improving electron transport, making $Ni_3V_2O_8$-NC an enhanced electrode material for energy storage applications.

Author contribution statement

Awatif Rashed Z. Almotairy: Contributed reagents, materials, analysis tools or data; Wrote the paper. BASHEER M. AL-MASWARI: Conceived and designed the experiments; Performed the experiments; Analyzed and interpreted the data; Contributed reagents, materials, analysis tools or data; Wrote the paper. Khaled Alkanad: Conceived and designed the experiments; Analyzed and interpreted the data; Wrote the paper. N. K. Lokanath: R. T. Radhika: Analyzed and interpreted the data. B. M. Venkatesha: analyzed and interpreted the data; Wrote the paper.

Data availability statement

Data will be made available on request.

Declaration of interest's statement

The authors declare no conflict of interest.

Declaration of competing interest

The authors declare that they have no known competing financial interests or personal relationships that could have appeared to influence the work reported in this paper.

Acknowledgment

Basheer M. Almaswari is thankful to the government of Yemen, Amran University, Amran, Yemen, and the University of Mysore, Mysore, India. All the authors are grateful to SAIF, IIT Bombay, and IIT Roorkee for carrying out the characterization of the research paper.

References

[1] A.M. Omer, Energy, environment and sustainable development, Renew. Sustain. Energy Rev. 12 (9) (2008) 2265–2300.

[2] K. Alkanad, et al., One-step hydrothermal synthesis of anatase TiO_2 nanotubes for efficient photocatalytic CO_2 reduction, ACS Omega (2022).
[3] K.K. Haldar, et al., *Construction of three-dimensional marigold flower-shaped $Ni_3V_2O_8$ for efficient solid-state supercapacitor applications*, Energy Storage (2022) e378.
[4] Y.A. Kumar, H.-J. Kim, Effect of time on a hierarchical corn skeleton-like composite of coo@zno as capacitive electrode material for high specific performance supercapacitors, Energies 11 (12) (2018) 3285.
[5] B.M. Al-Maswari, et al., Magnesium bismuth ferrite nitrogen-doped carbon nanomagnetic perovskite: synthesis and characterization as a high-performance electrode in a supercapacitor for energy storage, ACS Omega 8 (18) (2023) 16145–16157.
[6] A. Hezam, et al., *2D/1D MoS_2/TiO_2 heterostructure photocatalyst with a switchable CO_2 reduction product*, Small Methods 7 (1) (2023), 2201103.
[7] S. Zheng, et al., Transition-metal (Fe, Co, Ni) based metal-organic frameworks for electrochemical energy storage, Adv. Energy Mater. 7 (18) (2017), 1602733.
[8] G.S. Shekar, et al., Alkaline mediated sono-synthesis of surface oxygen-vacancies-rich cerium oxide for efficient photocatalytic CO_2 reduction to methanol, Surface. Interfac. (2022), 102389.
[9] X. Yuan, Y. Matsuyama, T.M. Chung, Synthesis of functionalized isotactic polypropylene dielectrics for electric energy storage applications, Macromolecules 43 (9) (2010) 4011–4015.
[10] J.-H. Yoon, et al., Highly efficient copper-cobalt sulfide nano-reeds array with simplistic fabrication strategy for battery-type supercapacitors, J. Energy Storage 32 (2020), 101988.
[11] M. Sethi, et al., Eco-friendly synthesis of porous graphene and its utilization as high performance supercapacitor electrode material, J. Alloys Compd. 799 (2019) 256–266.
[12] W.H. Low, et al., *Facile synthesis of graphene-$Zn_3V_2O_8$ nanocomposite as a high performance electrode material for symmetric supercapacitor*, J. Alloys Compd. 784 (2019) 847–858.
[13] X. He, et al., *Hierarchical $FeCo_2O_4$@NiCo layered double hydroxide core/shell nanowires for high performance flexible all-solid-state asymmetric supercapacitors*, Chem. Eng. J. 334 (2018) 1573–1583.
[14] Y.A. Kumar, et al., Facile synthesis of efficient construction of tungsten disulfide/iron cobaltite nanocomposite grown on nickel foam as a battery-type energy material for electrochemical supercapacitors with superior performance, J. Colloid Interface Sci. 609 (2022) 434–446.
[15] C. Bie, et al., *Graphite nanoplates firmly anchored with well-dispersed porous $Zn_3V_2O_8$ nanospheres: rational fabrication and enhanced lithium storage capability*, Electrochim. Acta 248 (2017) 140–149.
[16] M. Sethi, U.S. Shenoy, D.K. Bhat, Hassle-free solvothermal synthesis of NiO nanoflakes for supercapacitor application, Phys. B Condens. Matter 611 (2021), 412959.
[17] S. Vijayakumar, S.-H. Lee, K.-S. Ryu, Synthesis of $Zn_3V_2O_8$ Nanoplatelets for Lithium-Ion Battery and Supercapacitor Applications, 2015.
[18] M. Yang, et al., *Hierarchical ultrafine $Ni_3V_2O_8$ nanoparticles Anchored on rGO as high-performance anode Materials for lithium-ion batteries*, Energy Technol. 7 (8) (2019), 1800784.
[19] V. Soundharrajan, et al., *Bitter gourd-shaped $Ni_3V_2O_8$ anode developed by a one-pot metal-organic framework-combustion technique for advanced Li-ion batteries*, Ceram. Int. 43 (16) (2017) 13224–13232.
[20] B. Sambandam, et al., *$Ni_3V_2O_8$ nanoparticles as an excellent anode material for high-energy lithium-ion batteries*, J. Electroanal. Chem. 810 (2018) 34–40.
[21] C. Wang, et al., *Uniform nickel vanadate ($Ni_3V_2O_8$) nanowire arrays organized by ultrathin nanosheets with enhanced lithium storage properties*, Sci. Rep. 6 (1) (2016) 1–8.
[22] M. Wu, et al., *Graphene coated $Co_3V_2O_8$ micro-pencils for enhanced-performance in lithium ion batteries*, New J. Chem. 41 (19) (2017) 10634–10639.
[23] S. Lu, et al., *Ordered mesoporous carbon supported $Ni_3V_2O_8$ composites for lithium-ion batteries with long-term and high-rate performance*, J. Mater. Chem. 6 (16) (2018) 7005–7013.
[24] X. Li, et al., A first principles and experimental study on the influence of nitrogen doping on the performance of amorphous carbon films for proton exchange membrane fuel cells, Carbon 167 (2020) 219–229.
[25] V.V. Chaban, N.A. Andreeva, Structure, thermodynamic and electronic properties of carbon-nitrogen cubanes and protonated polynitrogen cations, J. Mol. Struct. 1149 (2017) 828–834.
[26] V.V. Chaban, O.V. Prezhdo, Nitrogen–nitrogen bonds undermine stability of N-doped graphene, J. Am. Chem. Soc. 137 (36) (2015) 11688–11694.
[27] M. Naushad, et al., Nickel ferrite bearing nitrogen-doped mesoporous carbon as efficient adsorbent for the removal of highly toxic metal ion from aqueous medium, Chem. Eng. J. 330 (2017) 1351–1360.
[28] B.M. Al-Maswari, et al., *Synthesis of perovskite bismuth ferrite embedded nitrogen-doped Carbon ($BiFeO_3$-NC) nanocomposite for energy storage application*, J. Energy Storage 44 (2021), 103515.
[29] S. Chandrasekaran, et al., Advanced opportunities and insights on the influence of nitrogen incorporation on the physico-/electro-chemical properties of robust electrocatalysts for electrocatalytic energy conversion, Coord. Chem. Rev. 449 (2021), 214209.
[30] Y.A. Kumar, K.D. Kumar, H.-J. Kim, *Facile preparation of a highly efficient $NiZn_2O_4$–NiO nanoflower composite grown on Ni foam as an advanced battery-type electrode material for high-performance electrochemical supercapacitors*, Dalton Trans. 49 (11) (2020) 3622–3629.
[31] Y.A. Kumar, et al., *A $MoNiO_4$ flower-like electrode material for enhanced electrochemical properties via a facile chemical bath deposition method for supercapacitor applications*, New J. Chem. 44 (2) (2020) 522–529.
[32] A. Karmakar, S.K. Srivastava, In situ fabricated nickel vanadate/N-doped reduced graphene oxide hybrid as an advanced electrocatalyst in alkaline hydrogen evolution reaction, J. Mater. Chem. 7 (25) (2019) 15054–15061.
[33] B.M. Al-Maswari, et al., *Nanomagnetic strontium ferrite nitrogen doped carbon ($SrFe_2O_4$-NC): synthesis, characterization and excellent supercapacitor performance*, J. Energy Storage 52 (2022), 104821.
[34] M.J. Gomez, et al., Highly efficient hybrid Ni/nitrogenated graphene electrocatalysts for hydrogen evolution reaction, ACS Omega 4 (1) (2019) 2206–2216.
[35] N. Roy, K.T. Leung, D. Pradhan, *Nitrogen doped reduced graphene oxide based Pt–TiO_2 nanocomposites for enhanced hydrogen evolution*, J. Phys. Chem. C 119 (33) (2015) 19117–19125.
[36] R. Kumar, et al., *Free-standing $Ni_3(VO_4)_2$ nanosheet arrays on aminated r-GO sheets for supercapacitor applications*, New J. Chem. 42 (2) (2018) 1243–1249.
[37] C. Sengottaiyan, et al., *$BiVO_4$/RGO hybrid nanostructure for high performance electrochemical supercapacitor*, J. Solid State Chem. 269 (2019) 409–418.
[38] W.H. Low, et al., *Facile solvothermal designing of graphene/$Ni_3V_2O_8$ nanocomposite as electrode for high performance symmetric supercapacitor*, J. Alloys Compd. 768 (2018) 995–1005.
[39] H. Fu, Z. Duan, G. Henkelman, *Computational study of structure and reactivity of oligomeric vanadia clusters supported on anatase and rutile TiO_2 surfaces*, J. Phys. Chem. C 119 (27) (2015) 15160–15167.
[40] T. Dhanasekaran, et al., *Gradient oxygen vacancies in $BiVO_4$ olive-seeds nanostructure for electrochemical supercapacitor applications*, Mater. Chem. Phys. 269 (2021), 124737.
[41] Y. Zhang, et al., *In-situ synthesis of three-dimensionally flower-like $Ni_3V_2O_8$@carbon nanotubes composite through self-assembling for high performance asymmetric supercapacitors*, J. Power Sources 455 (2020), 227985.
[42] F. Ghani, et al., *Facile one-step hydrothermal Synthesis of the rGO@$Ni_3V_2O_8$ interconnected hollow microspheres Composite for lithium-ion batteries*, Nanomaterials 10 (12) (2020) 2389.
[43] T. Ahamad, *$CoSe_2$@N-Doped graphene nanocomposite high-efficiency counter Electrode for dye-sensitized solar cells*, J. Inorg. Organomet. Polym. Mater. (2022) 1–10.
[44] A.H. Bashal, et al., *Synergistic effect of cocatalyst and S-scheme heterojunction over 2D/2D g-C_3N_4/MoS_2 heterostructure coupled Cu nanoparticles for selective photocatalytic CO_2 reduction to CO under visible light irradiation*, J. Environ. Chem. Eng. 11 (2) (2023), 109545.
[45] K. Thiagarajan, et al., *Synthesis of $Ni_3V_2O_8$@graphene oxide nanocomposite as an efficient electrode material for supercapacitor applications*, J. Solid State Electrochem. 22 (2) (2018) 527–536.
[46] E. Vesali-Kermani, A. Habibi-Yangjeh, S. Ghosh, *Efficiently enhanced nitrogen fixation performance of g-C_3N_4 nanosheets by decorating $Ni_3V_2O_8$ nanoparticles under visible-light irradiation*, Ceram. Int. 46 (15) (2020) 24472–24482.
[47] A. Rahdar, M. Aliahmad, Y. Azizi, NiO Nanoparticles: Synthesis and Characterization, 2015.

[48] S.D. Khairnar, V.S. Shrivastava, Facile synthesis of nickel oxide nanoparticles for the degradation of Methylene blue and Rhodamine B dye: a comparative study, J. Taibah Univ. Sci. 13 (1) (2019) 1108–1118.

[49] P. Augustine, Y. Narayana, N. Kalarickal, *Enhancement of room temperature magneto-electric coupling effect in perovskite-spinel (1−x) $BiFeO_{3-x}ZnFe_2O_4$ nanocomposites*, Mater. Today: Proc. 35 (2021) 436–439.

[50] S. Rakshit, et al., Controlled synthesis of spin glass nickel oxide nanoparticles and evaluation of their potential antimicrobial activity: a cost effective and eco friendly approach, RSC Adv. 3 (42) (2013) 19348–19356.

[51] S.S. Gc, et al., Surface defect engineered CeO_{2-x} by ultrasound treatment for superior photocatalytic H_2 production and water treatment, Catal. Sci. Technol. (2022).

[52] M.-C. Liu, et al., *Synthesis and characterization of $M_3V_2O_8$ (M= Ni or Co) based nanostructures: a new family of high performance pseudocapacitive materials*, J. Mater. Chem. 2 (14) (2014) 4919–4926.

[53] M. Liu, L.B. Kong, P. Zhang, Y.C. Luo, L. Kang, Porous wood carbon monolith for high-performance supercapacitors, Electrochim. Acta 60 (2012) 443–448.

[54] A. Ariharan, B. Viswanathan, V. Nandhakumar, Nitrogen doped graphene as potential material for hydrogen storage, Graphene 6 (2) (2017) 41–60.

[55] W. Ouyang, et al., Exploring the active sites of nitrogen-doped graphene as catalysts for the oxygen reduction reaction, Int. J. Hydrogen Energy 39 (28) (2014) 15996–16005.

[56] T. Ahamad, et al., N/S-doped carbon embedded with AgNPs as a highly efficient catalyst for the reduction of toxic organic pollutants, Mater. Lett. 264 (2020), 127310.

[57] L.N. Ramavathu, et al., *Synthesis and characterization of Nickel Metavanadate ($Ni_3V_2O_8$)-application as photocatalyst and supercapacitor*, Int. J. Nano Dimens. (IJND) 12 (4) (2021) 411–421.

[58] Y. Chen, et al., *Bandgap Engineering and oxygen Vacancies of $Ni_xV_2O_{5+x}$ (x= 1, 2, 3) for efficient visible light-driven CO_2 to CO with nearly 100% selectivity*, Solar RRL 6 (7) (2022), 2200099.

[59] Q. Zhou, Y. Gong, J. Lin, *Low temperature synthesis of sponge-like NiV_2O_6/C composite by calcining Ni-V-based coordination polymer for supercapacitor application*, J. Electroanal. Chem. 823 (2018) 80–91.

[60] K. Alkanad, et al., *Magnetic recyclable α-Fe_2O_3–Fe_3O_4/Co_3O_4–CoO nanocomposite with a dual Z-scheme charge transfer pathway for quick photo-Fenton degradation of organic pollutants*, Catal. Sci. Technol. 11 (9) (2021) 3084–3097.

[61] Y.A. Kumar, et al., *Self-supported Co_3O_4@Mo-Co_3O_4 needle-like nanosheet heterostructured architectures of battery-type electrodes for high-performance asymmetric supercapacitors*, Nanomaterials 12 (14) (2022) 2330.

[62] T. Purkait, et al., High-performance flexible supercapacitors based on electrochemically tailored three-dimensional reduced graphene oxide networks, Sci. Rep. 8 (1) (2018) 1–13.

[63] X. Liu, J. Wang, G. Yang, *In situ growth of the $Ni_3V_2O_8$@ PANI composite electrode for flexible and transparent symmetric supercapacitors*, ACS Appl. Mater. Interfaces 10 (24) (2018) 20688–20695.

[64] X. Liu, J. Wang, G. Yang, Transparent, flexible, and high-performance supercapacitor based on ultrafine nickel cobaltite nanospheres, Appl. Phys. A 123 (7) (2017) 1–11.

[65] S. Venkateswarlu, et al., *Fe_3O_4 nano assembly embedded in 2D-crumpled porous carbon sheets for high energy density supercapacitor*, Chem. Eng. J. 420 (2021), 127584.

[66] B.-A. Mei, et al., Physical interpretations of Nyquist plots for EDLC electrodes and devices, J. Phys. Chem. C 122 (1) (2018) 194–206.

[67] Y.-S. Lee, et al., *$CoCu_2O_4$ nanoflowers architecture as an electrode material for battery type supercapacitor with improved electrochemical performance*, Nano-Structures & Nano-Objects 24 (2020), 100618.

[68] W.H. Low, Hybridisation of Mixed Transition Metal Oxide with Graphene as Advanced Electrode Material for Symmetric Supercapacitor Application, University of Nottingham, 2021.

[69] M. Sethi, et al., *Facile solvothermal synthesis of $NiFe_2O_4$ nanoparticles for high-performance supercapacitor applications*, Front. Mater. Sci. 14 (2020) 120–132.

[70] M. Sethi, U.S. Shenoy, D.K. Bhat, Simple solvothermal synthesis of porous graphene-NiO nanocomposites with high cyclic stability for supercapacitor application, J. Alloys Compd. 854 (2021), 157190.

[71] R. Kumar, P. Rai, A. Sharma, *3D urchin-shaped $Ni_3(VO_4)_2$ hollow nanospheres for high-performance asymmetric supercapacitor applications*, J. Mater. Chem. 4 (25) (2016) 9822–9831.

[72] A.K. Yedluri, H.-J. Kim, *Wearable super-high specific performance supercapacitors using a honeycomb with folded silk-like composite of $NiCo_2O_4$ nanoplates decorated with NiMoO 4 honeycombs on nickel foam*, Dalton Trans. 47 (43) (2018) 15545–15554.

[73] S.M. Alshehri, et al., Nitrogen-doped cobalt ferrite/carbon nanocomposites for supercapacitor applications, Chemelectrochem 4 (11) (2017) 2952–2958.

[74] K.K. Haldar, et al., *Construction of three-dimensional marigold flower-shaped $Ni_3V_2O_8$ for efficient solid-state supercapacitor applications*, Energy Storage 4 (6) (2022) e378.